

HIGHER ORDER TEAGER-KAISER OPERATORS FOR IMAGE ANALYSIS: PART I - A MONOCOMPONENT IMAGE DEMODULATION.

El Hadji S. Diop, A. O. Boudraa

Groupe ASM, Ecole Navale
IRENav / E³I²-EA3876, ENSIETA
Ecole Navale, Lanvéoc-Poulmic
29240 Brest—Armées, France.

Fabien Salzenstein

Laboratoire Iness, CNRS/STIC-UPR
Université Louis Pasteur
23 rue du Loess, BP 20 CR
67037 Strasbourg Cedex 2, France.

ABSTRACT

We present in this paper a new narrowband image demodulation method. Our approach is based on the 2D higher order Teager-Kaiser operators (HOTKO). We show that the introduction of higher orders in the Teager-Kaiser operator, improves a lot the demodulation results, in comparison to the Discrete Energy Separation Algorithm (DESA) and the Analytic Image (AI) method. More precisely, for synthetic images, we show that the approximation errors on both the amplitude and the frequency components are much more lower with our proposed demodulation method than the DESA and the AI method. Moreover, it turns out that for the presented real images, the algorithm is so efficient, especially the amplitude counterpart, that it tracks the most important parts in images, and segments the regions of interest. We show how the algorithm could be used in Sonar images for extracting mines' shadows, which is very important for both military and civil applications.

Index Terms— Amplitude modulation, frequency modulation, nonlinear filters, operators.

I. INTRODUCTION

The Teager-Kaiser Energy Operator (TKEO) was initially introduced by Kaiser [1] for speech recognition, and later on extended to the two-dimensional (2D) case by Yu et al. [2]. Demodulating a signal of any dimension consists in finding the FM (Frequency Modulation) and the AM (Amplitude Modulation) components. For a given image, the AM component gives information about textures' contrast, that is the intensity disparity between the dark and bright textures. The FM part tells us about the local texture orientation, the image granularity and the edges in the image. AM-FM image modeling have been applied in many image processing areas [3], [4], [5], [6]. Many demodulation algorithms have been proposed. We have the ESA (Energy Separation Algorithm) and its discrete version, the DESA [7] and the 2D ESA for images [8]. Both the ESA and the 2D ESA rely on the TKEO [7], [8]. Narrowband images, modeled as 2D spatial AM-FM signals, can be demodulated by the 2D

ESA [8]. Another image demodulation approach based on the AI was proposed by Havlicek [9]. His approach relies on the 2D Hilbert transform. One major weakness of all these demodulation techniques, is that they all work only for narrow band and locally constant amplitude signals. HOTKO for 1D signals, which generalize the TKEO, were first introduced by Maragos and Potamianos [10]. In [11], Salzenstein et al. presented discrete versions of HOTKO, and showed that the demodulation results, especially the AM components, are qualitatively better than the ones obtained with the TKEO and other different demodulation methods. Motivated by the works in [11], [12], we explore in this paper the discrete 2D HOTKO, in order to get, as for the 1D case, better image demodulation results.

II. A NARROWBAND IMAGE DEMODULATION BASED ON HOTKO.

Let I be a discrete image. For simplicity, we also denote by I its continuous interpolate. The image and its interpolate will be distinguished by their arguments: if we use the notation $I(k, l)$, then I is the discrete image; and for $I(x_1, x_2)$, I represents the interpolated image. 2D HOTKO will be extrapolated from:

$$\begin{aligned} \phi_2 [I(x_1, x_2)] = & \left[\left(\frac{\partial I}{\partial x_1} \right)^2 - I \frac{\partial^2 I}{\partial x_1^2} \right] + \left[\left(\frac{\partial I}{\partial x_2} \right)^2 - I \frac{\partial^2 I}{\partial x_2^2} \right] \\ & + 2 \left[\left(\frac{\partial I}{\partial x_1} \frac{\partial I}{\partial x_2} \right) - I \frac{\partial^2 I}{\partial x_1 \partial x_2} \right] \quad (1) \end{aligned}$$

The first two terms correspond to the 2D TKEO [2], [13]. The last one constitutes the major difference. It represents the image's energy correlation between the horizontal and vertical directions. Equation (1) can be rewritten as:

$$\phi_2 [I(x_1, x_2)] = \{ \Lambda [I(x_1, x_2)] \}^2 - I(x_1, x_2) \cdot \Lambda^2 [I(x_1, x_2)] \quad (2)$$

where $\Lambda(I) = \frac{\partial I}{\partial x_1} + \frac{\partial I}{\partial x_2}$. The generalization at any order k is given in [12] by:

$$\begin{aligned} \phi_k [I(x_1, x_2)] &= \Lambda [I(x_1, x_2)] \cdot \Lambda^{k-1} [I(x_1, x_2)] \\ &\quad - I(x_1, x_2) \cdot \Lambda^k [I(x_1, x_2)] \end{aligned} \quad (3)$$

We prove by recurrence that for all $k > 3$, we have:

$$\begin{aligned} \phi_k [I(x_1, x_2)] &= \partial_1 \{ \phi_{k-1} [I(x_1, x_2)] \} + \partial_2 \{ \phi_{k-1} [I(x_1, x_2)] \} \\ &\quad - \phi_{k-2} [\partial_1 I(x_1, x_2) + \partial_2 I(x_1, x_2)], \end{aligned} \quad (4)$$

where, for any function f of class $C^m(\mathbb{R}^2)$,

$\partial_{1^p 2^q}^m (f) = \frac{\partial^m f}{\partial x_1^p \partial x_2^q} (x_1, x_2)$ with $p+q = m$. Let's consider an AM-FM image:

$$I(x_1, x_2) = a(x_1, x_2) \cos(\Omega_1 \cdot x_1 + \Omega_2 \cdot x_2). \quad (5)$$

For a pure 2D sinusoid (i.e $a(x_1, x_2) = cste$), applying I to ϕ_2 yields:

$$\phi_2 [I(x_1, x_2)] = [a(x_1, x_2)]^2 (\Omega_1 + \Omega_2)^2 \quad (6)$$

Thanks to [2], we have:

$$\phi_3 [I(x_1, x_2)] = 0 \quad (7)$$

$$\phi_4 [I(x_1, x_2)] = -[a(x_1, x_2)]^2 (\Omega_1 + \Omega_2)^4 \quad (8)$$

We also get:

$$\begin{aligned} \phi_2 [\partial_1 I(x_1, x_2) - \partial_2 I(x_1, x_2)] &= \\ [a(x_1, x_2)]^2 (\Omega_1 - \Omega_2)^2 (\Omega_1 + \Omega_2)^2 \end{aligned} \quad (9)$$

$$\begin{aligned} \phi_2 [\partial_1 I(x_1, x_2) + \partial_2 I(x_1, x_2)] &= \\ [a(x_1, x_2)]^2 (\Omega_1 + \Omega_2)^2 (\Omega_1 + \Omega_2)^2. \end{aligned} \quad (10)$$

We use $I_1(k, l) = \frac{1}{2} [I(k+1, l) - I(k-1, l)]$, $I_2(k, l) = \frac{1}{2} [I(k, l+1) - I(k, l-1)]$ and $I_{12}(k, l) = \frac{1}{2} [I_2(k+1, l) - I_2(k-1, l)]$ as the discretization schemes of $\frac{\partial I}{\partial x_1}$, $\frac{\partial I}{\partial x_2}$ and $\frac{\partial^2 I}{\partial x_1 \partial x_2}$, respectively. Then, equation(1) is discretized as follow:

$$\begin{aligned} \Psi_2 [I(k, l)] &= [2 [I(k, l)]^2 - I(k-1, l) I(k+1, l) \\ &\quad - I(k, l-1) I(k, l+1)] + 2 [I_1(k, l) I_2(k, l) \\ &\quad - I(k, l) I_{12}(k, l)]. \end{aligned}$$

Let $I(k, l) = a(k, l) \cos(\Omega_1 k + \Omega_2 l)$ be a discrete image with a slowly varying amplitude. Then, thanks to [2] and under realistic assumptions [8], we have:

$$\Psi_2 [I(k, l)] \approx [a(k, l)]^2 (\sin(\Omega_1) + \sin(\Omega_2))^2 \quad (11)$$

$$\Psi_3 [I(k, l)] = 0 \quad (12)$$

$$\Psi_4 [I(k, l)] \approx -[a(k, l)]^2 (\sin(\Omega_1) + \sin(\Omega_2))^4 \quad (13)$$

We have also the relations $\forall i = 1, 2$:

$$\Psi_2 [I_i(k, l)] \approx [a(k, l)]^2 [\sin(\Omega_i)]^2 (\sin(\Omega_1) + \sin(\Omega_2))^2 \quad (14)$$

$$\begin{aligned} \Psi_2 [I_{12}(k, l)] &\approx [a(k, l)]^2 [\sin(\Omega_1)]^2 [\sin(\Omega_2)]^2 \times \\ &\quad (\sin(\Omega_1) + \sin(\Omega_2))^2 \end{aligned} \quad (15)$$

$$\Psi_4 [I_i(k, l)] \approx -[a(k, l)]^2 [\sin(\Omega_i)]^2 (\sin(\Omega_1) + \sin(\Omega_2))^4 \quad (16)$$

$$\begin{aligned} \Psi_4 [I_{12}(k, l)] &\approx -[a(k, l)]^2 [\sin(\Omega_1)]^2 [\sin(\Omega_2)]^2 \cdot \\ &\quad (\sin(\Omega_1) + \sin(\Omega_2))^4 \end{aligned} \quad (17)$$

We finally get the AM and FM estimates respectively denoted by $\hat{a}(k, l)$, $\hat{\Omega}_1$ and $\hat{\Omega}_2$, by combining equations (11-17). Thus:

$$|\hat{a}(k, l)| = \sqrt{\frac{\Psi_2 [I_1(k, l)] \cdot \Psi_2 [I_2(k, l)]}{-\Psi_4 [I_{12}(k, l)]}} \quad (18)$$

$$|\hat{\Omega}_1(k, l)| = \arcsin \sqrt{\frac{\Psi_2 [I_{12}(k, l)]}{\Psi_2 [I_2(k, l)]}} \quad (19)$$

$$|\hat{\Omega}_2(k, l)| = \arcsin \sqrt{\frac{\Psi_2 [I_{12}(k, l)]}{\Psi_2 [I_1(k, l)]}} \quad (20)$$

Using equations (4) and (7) yields:

$$\phi_4 [I(x_1, x_2)] = -\phi_2 [\partial_1 I(x_1, x_2) + \partial_2 I(x_1, x_2)]$$

Finally, equation (18) can be rewritten as:

$$|\hat{a}(k, l)| = \sqrt{\frac{\Psi_2 [I_1(k, l)] \cdot \Psi_2 [I_2(k, l)]}{\Psi_2 [I_{12}^1(k, l) + I_{12}^2(k, l)]}} \quad (21)$$

where $I_{12}^1(k, l) = \frac{1}{2} [I_{12}(k+1, l) - I_{12}(k-1, l)]$, and $I_{12}^2(k, l) = \frac{1}{2} [I_{12}(k, l+1) - I_{12}(k, l-1)]$.

From now on, formulas (18-21) will be referred to as DHODA (Discrete Higher Order Demodulation Algorithm).

III. NUMERICAL RESULTS.

The DHODA is applied to both synthetic and real mono-component images. We first apply the proposed algorithm on the synthetic image I defined by:

$$\begin{aligned} I(m, n) &= 0.5 [1 + 0.5 \cos(m\pi/30 + n\pi/50)] \cos[m\pi/3 \\ &\quad + n\pi/5 + 2 \cos(m\pi/30) \cos(n\pi/50 + \pi/2)] \end{aligned}$$

where $m, n \in \{1, 2, \dots, 100\}$.

AM and FM components of I obtained with the DHODA are shown in Fig. 1. Because the DESA [8] gives qualitatively the same demodulation results, it was better to evaluate the demodulation errors with the two different demodulation methods. Errors are calculated according to the L^2 norm, the MSE (Minimum Squared Error) and their relative variances. As shown in Table 1, approximation errors are much more lower with the DHODA than the DESA [8].

The DHODA is also applied on some real narrowband images, the square image (Fig. 2-(a)) and two sonar images (Figs. 2-(e) and 2-(i)). In addition to the conditions of narrow band and slowly varying amplitude, we add the hypothesis

of a null mean. Practically, we subtract from the image its mean. As also noticed in [8], some pixels' energy yields negative values. Maragos and Bovik [8] suggested to set all negative values to zero. In the presented work, we apply a window averaging scheme in the neighborhood of the pixel that gives a negative value. Also, before demodulating the real monocomponent images, we apply a median filter as a pre-processing. Just pointing out that the same pre-processing is applied to all the demodulation techniques that will be discussed below. The AM components of the square image obtained also with the DESA [8] and the AI [9] are shown in Fig. 2. As one notices, the AM component obtained with the DHODA (Fig. 2-(d)) captures the dark square and segments it. In Figs. 2-(b) and 2-(c), we display the AM parts obtained respectively with the DESA [8] and the AI [9]. Remark that the segmentation of the dark square could be a difficult task for other segmentation techniques. To illustrate that fact, we use an image thresholding method for a segmentation issue. Fig. 3-(b) shows the thresholded image based on the bimodal histogram (Fig. 3-(a)). Notice the noise artefacts on the dark square, the image background and the image borders.

There are three major parts in the sonar images (Figs. 2-(e) and 2-(i)): the echos, the mines' shadows and the sea-bottom reverberations. The AM components are again conclusive for the segmentation of the main parts in such images, the mines' shadows (Figs. 2-(h) and 2-(l)). Figs. 2-(f) and 2-(j), and Figs. 2-(g) and 2-(k) show the AM parts obtained respectively with the DESA [8] and the AI [9], for the first and second sonar image (Figs. 2-(e) and 2-(i)), respectively. We recall that the AM component holds the information about textures' contrast, that is the intensity disparity between the dark and bright textures. We do not expect the AM to segment any part in the image while using the DESA [8] or the AI [9], but we just put forward the additional and relevant texture information brought out by the 2D HOTKO. To display the FM counterparts, we use needle diagram plottings, which are much more expressive [9], [14]. The diagrams are composed of arrows. For every pixel, an arrow is drawn at the pixel's neighborhood for clarity. The arrow originates from that pixel, and terminates by an arrowhead. The length of the arrow is inversely proportional to the FM's magnitude. With this displaying style, image frequencies make much more sense and are much more conclusive, in comparison to the Fourier transform. For the square image (Fig. 2-(a)), we have, as expected, small arrows of same orientations all around the black square, which traduce high frequencies area (Fig. 4-(a)). And we have large arrows with also the same orientations inside the black square, which means low frequencies (Fig. 4-(a)). That is coherent because it is an homogeneous zone. Because of the texture characteristics of the sonar images (Figs. 2-(e) and 2-(i)), the FM components are composed, as expected again, of very small arrows all around the mines' shadows

Table I. DHODA and DESA approximation errors.

	MSE(a, \hat{a})	$\ a - \hat{a}\ _2$	$var\left(\frac{a - \hat{a}}{a}\right)$
DESA	0.0119	10.9278	0.0415
DHODA	$9.9617 \cdot 10^{-4}$	3.1562	0.0044
	MSE($\Omega_1, \hat{\Omega}_1$)	$\ \Omega_1 - \hat{\Omega}_1\ _2$	$var\left(\frac{\Omega_1 - \hat{\Omega}_1}{\Omega_1}\right)$
DESA	0.0483	21.9681	0.0418
DHODA	0.0092	9.5979	0.0093
	MSE($\Omega_2, \hat{\Omega}_2$)	$\ \Omega_2 - \hat{\Omega}_2\ _2$	$var\left(\frac{\Omega_2 - \hat{\Omega}_2}{\Omega_2}\right)$
DESA	0.0164	12.8214	0.0387
DHODA	0.0059	7.6501	0.0146

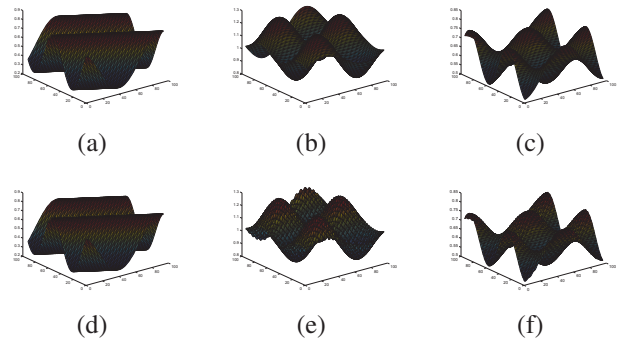


Fig. 1. Real: AM (a). Horizontal FM (b). Vertical FM (c). Estimates: AM (d). Horizontal FM (e). Vertical FM (f).

(Figs. 4-(b) and 4-(c)). This indicates very high frequencies in those zones, which makes sense. On the contrary, we have large arrows in the areas corresponding to the mines' shadows (Figs. 4-(b) and 4-(c)). This means that we have low frequencies in those areas which also makes sense, because of the homogeneity of those zones.

IV. CONCLUSION

A new algorithm based on 2D HOTKO is brought out. The proposed DHODA performs far better than the DESA [8]. Indeed, as confirmed in Table 1, approximation errors on both the amplitude and frequencies are much more lower. In addition, for the real monocomponent images used in our experiments, the 2D HOTKO bring relevant additional texture information that cannot be carried out by the TKEO. AM obtained with the DHODA capture the most important part in the sonar images presented, and segment the mines' shadows. The segmentation of mines' shadow is very important for civil and military applications. We finally show the coherence between frequencies and images.

ACKNOWLEDGEMENTS

We are grateful to Joseph P. Havlicek and Chuong T. Nguyen, both at The University of Oklahoma at Norman,

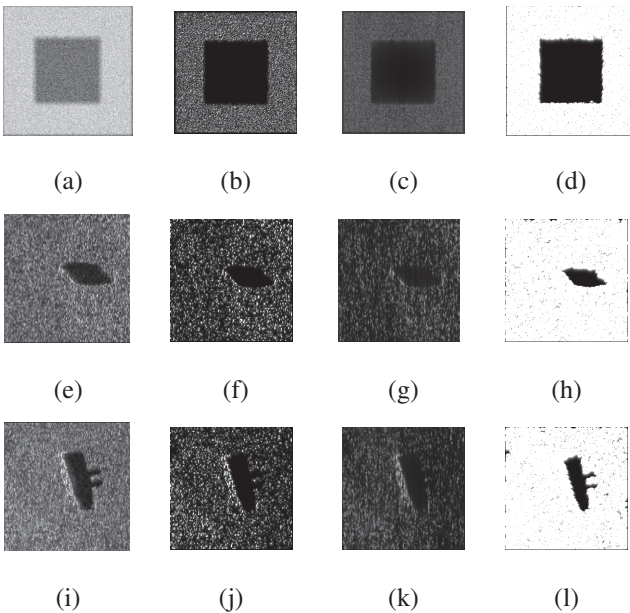


Fig. 2. From left to right: first column: original images; second: AM with DESA; third: AM with AI; fourth: AM with DHODA.

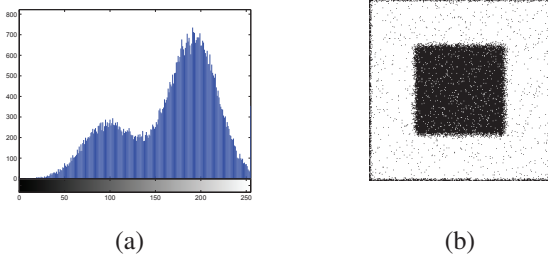


Fig. 3. Histogram of the square image (a). Image thresholded (b).

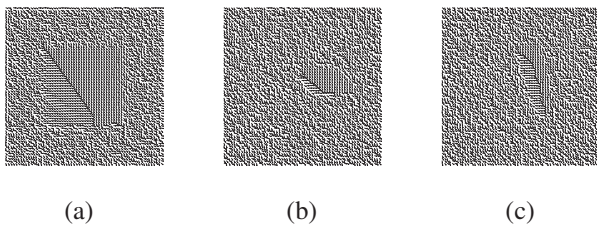


Fig. 4. FM modulus needle diagram plottings of Figures: 2-(a) (a). 2-(e) (b). 2-(i) (c).

for providing the needle diagram codes.

V. REFERENCES

- [1] J. F. Kaiser, "On a simple algorithm to calculate the 'energy' of a signal," in *IEEE ICASSP*, April 1990, pp. 381–384.
- [2] T. H. Yu, S. K. Mitra, and J. F. Kaiser, "A novel nonlinear filter for image enhancement," in *SPIE/SPSE Symp. on Electronic Imaging: Science and Technology*, 1991, pp. 303–309.
- [3] I. Kokkinos, G. Evangelopoulos, and P. Maragos, "Advances in texture analysis: energy dominant component & multiple hypothesis testing," in *IEEE ICIP*, Singapore, 24–27 October 2004, pp. 1509–1512.
- [4] A. Sofou, G. Evangelopoulos, and P. Maragos, "Coupled geometric and texture pde-based segmentation," in *IEEE ICIP*, vol. II, Genova, Italy, September 2005, pp. 650–653.
- [5] M. S. Pattichis and A. C. Bovik, "Analyzing image structure by multidimensional frequency modulation," *IEEE Trans. PAMI*, vol. 29, no. 5, pp. 753–766, May 2007.
- [6] I. Kokkinos, G. Evangelopoulos, and P. Maragos, "Texture analysis and segmentation using modulation features, generative models and weighted curve evolution," *IEEE Trans. on PAMI*, vol. 31, no. 1, pp. 142–157, January 2009.
- [7] P. Maragos, J. F. Kaiser, and T. F. Quatieri, "Energy separation in signal modulations with application to speech analysis," *IEEE Trans. on Sig. Proc.*, vol. 41, no. 10, pp. 3024–3051, October 1993.
- [8] P. Maragos and A. C. Bovik, "Image demodulation using multidimensional energy separation," *Opt. Soc. Am. A*, vol. 12, no. 9, pp. 1867–1876, September 1995.
- [9] J. P. Havlicek, "Am-fm image models," Ph.D. dissertation, The University of Texas at Austin, 1996.
- [10] P. Maragos and A. Potamianos, "Higher order differential energy operators," *IEEE Trans. on Sig. Proc.*, vol. 2, no. 8, pp. 152–154, August 1995.
- [11] F. Salzenstein, P. Montgomery, A. Benatmane, and A. Boudraa, "2d discrete high order energy operators for surface profiling using white light interferometry," in *IEEE ISSPA*, vol. 1, 2003, pp. 601–604.
- [12] A. Boudraa, F. Salzenstein, and J. Cexus, "Two-dimensional continuous higher-order energy operators," *Optical Engineering*, pp. 7001–7010, 2005.
- [13] P. Maragos, J. F. Kaiser, and T. F. Quatieri, "On amplitude and frequency demodulations using energy operators," *IEEE Trans. on Sig. Proc.*, vol. 41, no. 4, pp. 1532–1550, April 1993.
- [14] J. P. Havlicek, P. C. Tay, and A. C. Bovik, *Handbook of Image and Video Processing*, 2nd ed. A. Bovik, 2005, ch. 4.4, pp. 377–395.